

Splitting Fermi Surfaces and Heavy Electronic States in Non-Centrosymmetric $\text{U}_3\text{Ni}_3\text{Sn}_4$

Arvind Maurya¹, Hisatomo Harima², Ai Nakamura¹, Yusei Shimizu¹, Yoshiya Homma¹, DeXin Li¹,
Fuminori Honda¹, Yoshiki J. Sato¹, and Dai Aoki^{1*}

¹*Institute for Materials Research, Tohoku University, Oarai, Ibaraki 311-1313, Japan*

²*Graduate School of Science, Kobe University, Kobe 657-8501, Japan*

We report the single-crystal growth of the non-centrosymmetric paramagnet $\text{U}_3\text{Ni}_3\text{Sn}_4$ by the Bridgman method and the Fermi surface properties detected by de Haas–van Alphen (dHvA) experiments. We have also investigated single-crystal $\text{U}_3\text{Ni}_3\text{Sn}_4$ by single-crystal X-ray diffraction, magnetization, electrical resistivity, and heat capacity measurements. The angular dependence of the dHvA frequencies reveals many closed Fermi surfaces, which are nearly spherical in topology. The experimental results are in good agreement with local density approximation (LDA) band structure calculations based on the $5f$ -itinerant model. The band structure calculation predicts many Fermi surfaces, mostly with spherical shape, derived from 12 bands crossing the Fermi energy. To our knowledge, the splitting of Fermi surfaces due to the non-centrosymmetric crystal in $5f$ -electron systems is experimentally detected for the first time. The temperature dependence of the dHvA amplitude reveals a large cyclotron effective mass of up to $35 m_0$, indicating the heavy electronic state of $\text{U}_3\text{Ni}_3\text{Sn}_4$ due to the proximity of the quantum critical point. From the field dependence of the dHvA amplitude, a mean free path of conduction electrons of up to 1950 \AA is detected, reflecting the good quality of the grown crystal. The small splitting energy related to the antisymmetric spin-orbit interaction is most likely due to the large cyclotron effective mass.

1. Introduction

Uranium compounds have been extensively studied owing to the intriguing nature of their $5f$ electrons giving rise to anomalous effects such as unconventional superconductivity, the coexistence of ferromagnetism and superconductivity, heavy-fermion behavior, anisotropic hybridization, local and itinerant magnetism, hidden order, and multipolar interactions.^{1–5)} The $5f$ electrons in uranium compounds may behave as itinerant as well as localized nature unlike the rather extreme cases of lanthanides (localized) and d -transition metals (itinerant). In the last few decades, non-centrosymmetric materials have attracted condensed matter physicists owing to their potential to exhibit anomalous behavior, for instance, mixed pair wave unconventional superconductivity, magnetic skyrmion lattices, multipolar ordering, and chiral fermiology. Spin-orbit coupling (SOC) plays an important role in such compounds by introducing splitting in otherwise spin-degenerate bands. Since the strength of SOC increases with the atomic number, non-centrosymmetric materials containing heavy elements such as uranium are promising candidates for interesting phenomena introduced by the confluence of SOC and the semi-itinerant character of $5f$ electrons. The de Haas–van Alphen (dHvA) effect, being an indispensable tool to explore the topology of Fermi surfaces, plays a crucial role in demystifying such an effect, because the splitting of Fermi surfaces due to SOC in a non-centrosymmetric material is directly detected from a microscopic viewpoint.

Many $\text{U}_3\text{T}_3\text{X}_4$ non-centrosymmetric uranium compounds with the cubic crystal structure (space group: #220, $I\bar{4}3d$, T_d^6) exist, namely $\text{U}_3\text{T}_3\text{Sn}_4$ ($\text{T} = \text{Pt, Ni, Au, Cu}$), $\text{U}_3\text{T}_3\text{Bi}_4$ ($\text{T} = \text{Rh, Ni}$), and $\text{U}_3\text{T}_3\text{Sb}_4$ ($\text{T} = \text{Pt, Pd, Ni, Cu, Co, Rh, Ir}$), possessing a rich variety of their properties: itinerant ferromagnet, metal, semiconductor, and heavy-fermion be-

havior.^{6–14)} However, most of them are either semiconducting [$\text{U}_3\text{Ni}_3\text{Bi}_4$, $\text{U}_3(\text{Pd,Pt,Ni})_3\text{Sb}_4$] or possess large residual scattering, for example, the residual resistivities, $c \rho_0$ of $\text{U}_3\text{Au}_3\text{Sn}_4$, $\text{U}_3\text{Rh}_3\text{Bi}_4$, $\text{U}_3\text{Co}_3\text{Sb}_4$, $\text{U}_3\text{Cu}_3\text{Sn}_4$, and $\text{U}_3\text{Cu}_3\text{Sb}_4$ are 500, 150, 300, 800, and $180 \mu\Omega \cdot \text{cm}$, respectively.^{8–11)} Nevertheless, $\text{U}_3\text{Ni}_3\text{Sn}_4$ and $\text{U}_3\text{Pt}_3\text{Sn}_4$ exhibit good values of ρ_0 ($< 5 \mu\Omega \cdot \text{cm}$) and the residual resistivity ratio (> 200) even in their polycrystalline samples,^{7,8)} making them suitable for quantum oscillation studies. Moreover, their paramagnetic ground state rules out the additional complexity in the band structure arising in the magnetically ordered state due to the formation of a magnetic Brillouin zone. The metallic or semiconducting behavior in this homologous series has been proposed to be governed by the electron count, charge balance, hybridization strength, and the intricate band structure.

Note that none of the aforementioned compounds have been explored in terms of detailed Fermi surface properties. However, Inada et al. have studied structurally related ferromagnets U_3As_4 ($T_C = 198 \text{ K}$) and U_3P_4 ($T_C = 138 \text{ K}$) by dHvA and magnetoresistance measurements.¹⁵⁾ Most of the dHvA branches in U_3X_4 ($\text{X} = \text{P, As}$) can be qualitatively explained by the spin-polarized $5f$ -itinerant band model. An enhancement of the cyclotron effective mass up to $70 m_0$ ($33 m_0$) in U_3As_4 (U_3P_4) is in consonance with the Sommerfeld coefficient of 83 (90) $\text{mJ}/(\text{mol-U K}^2)$. The magnetoresistance measurements confirmed the compensation of charge carriers in both metals and the existence of open orbits in U_3P_4 .

$\text{U}_3\text{Ni}_3\text{Sn}_4$ is described as a heavy-fermion paramagnet located at the verge of the antiferromagnetic quantum critical point with the negative critical pressure of -0.04 GPa .^{12,16–18)} From low-temperature specific heat measurements, it is suggested that the crossover from the non-Fermi liquid to the Fermi liquid state occurs below 0.4 K .¹³⁾ Upon applying pressure, the Fermi liquid state is recovered in a wide tempera-

*aoki@imr.tohoku.ac.jp

ture range.¹⁶⁾ A photoemission study by Takabatake et al. indicated that hybridization of the partially filled Ni 3*d* bands with the U 5*f* states may lead to the delocalization of the 5*f* electrons in U₃Ni₃Sn₄.¹⁹⁾ On the other hand, Endstra et al. demonstrated a continuous transformation from metallic to semiconducting behavior by substituting Sn by Sb, establishing the importance of Sn 5*p* electrons in the itineracy of U 5*f* orbitals.²⁰⁾ NMR studies reveal a crossover from localized to heavy-fermion character of the U 5*f* electrons in U₃Ni₃Sn₄.²¹⁾ as the temperature is lowered. Bremsstrahlung isochromat spectroscopy suggests that the hybridization of U 5*f* with Ni 3*d* and Sn 5*p* states as well as the Coulomb repulsion between the 5*f*-electrons is non-negligible.²²⁾ These findings suggest that the intricate correlations of electron orbitals drive U₃Ni₃Sn₄ to a heavy-fermion paramagnetic metal.

In order to clarify the electronic state of U₃Ni₃Sn₄, we carried out dHvA experiments in addition to magnetic susceptibility, magnetization, resistivity, and heat capacity measurements using a high-quality single crystal grown by the Bridgman method with a large residual resistivity ratio of RRR \sim 300. The detected Fermi surfaces are nearly spherical in topology with large cyclotron effective masses, indicating a heavy electronic state. The results are in reasonably good agreement with local density approximation (LDA) band calculations based on the 5*f*-itinerant model. The splitting of Fermi surfaces is detected because of the SOC owing to the lack of inversion symmetry in the crystal structure. The small splitting energies are probably due to the heavy cyclotron effective masses.

2. Experimental Procedure

We have utilized the Bridgman method to grow U₃Ni₃Sn₄ single crystals. A polycrystalline ingot of U₃Ni₃Sn₄ with a stoichiometric amount of each element was prepared in a tetra arc furnace before sealing it inside a tungsten Bridgman crucible in argon atmosphere. The sealed tungsten crucible was placed in a vertical tube furnace with a precalibrated temperature and thermal gradient profile. Argon gas was continuously flowed to avoid the oxidation of the crucible. The temperature inside the furnace was raised to 1350 °C in 12 h, and maintained at this temperature for another 12 h to ensure complete melting of the charge inside the crucible. After that, it was cooled to 900 °C at a rate of 4 °C/h then to 600 °C at a faster rate of 30 °C/h and finally to room temperature at 60 °C/h.

Clear Laue diffraction spots indicated the good quality of the grown crystal. However, it also turned out that the lump in the crucible after crystal growth contained several domains. Monodomain crystals were isolated by means of Laue photographs and a spark cutter. The maximum grain size was approximately $3 \times 2 \times 1$ mm³. Laue photographs were taken from all sides of the isolated crystal to ensure that it was a monodomain. The phase purity was confirmed by powder X-ray diffraction. Moreover, single-crystal X-ray diffraction was performed to refine the lattice parameters and atomic positions, which were subsequently used as the input in the band structure calculations.

The electrical resistivity in the temperature range 300–0.2 K was measured by a laboratory-built adiabatic demagnetization refrigerator (ADR) coupled with a Quantum Design physical property measurement system (QD PPMS). Heat capacity and magnetization measurements were carried out in

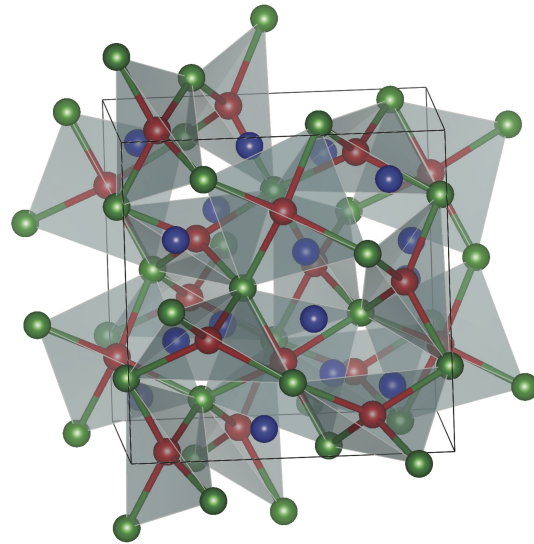


Fig. 1. (Color online) Crystal structure of U₃Ni₃Sn₄. Corner-sharing tetrahedra represent the crystallographically rigid network of U (red) and Ni (green) atoms placed at special crystallographic sites, while Sn atoms (blue) occupy a general position.

the QD PPMS and a QD magnetic property measurement system (MPMS), respectively. The dHvA measurements at low temperatures down to 35 mK and at high fields up to 147 kOe were carried out in a top-loading dilution refrigerator using a standard field modulation technique.

3. Results and Discussion

U₃Ni₃Sn₄ crystallizes in an Y₃Au₃Sb₄-type non-centrosymmetric body-centered cubic structure, which is a “filled up” version of the Th₃P₄-type structure,⁶⁾ as shown in Fig. 1. In order to determine the crystallographic parameters of U₃Ni₃Sn₄, we performed single-crystal X-ray diffraction at room temperature and analyzed the data by least-squares refinement. The results are summarized in Table I and II. The lattice parameter was determined to be $a = 9.3575(4)$ Å. In U₃Ni₃Sn₄ crystal, U and Ni atoms occupy the Wyckoff sites 12*a* and 12*b*, respectively, of space group $I\bar{4}3d$ (#220, T_d^6) possessing fourfold rotational symmetry. Note that these sites have fixed special crystallographic positions and form a rigid network of sites coordinated tetrahedrally with respect to each other. Sn atoms are placed at the site labeled as 16*c* having threefold axial symmetry along $\langle 111 \rangle$. The position of Sn atoms is specified by a single variable identical for *x*, *y*, and *z* atomic coordinates. The fractional coordinate for the Sn position is found to be 0.0820(2). The obtained lattice parameter and fractional coordinates are close to the previously reported values.^{6, 12)} Although the unit cell is large, the smallest distance between U atoms, d_{U-U} , is merely 4.377 Å. The rather small values of *R*1 and *wR*2 give credence to the correctness of our refined parameters over those in previous reports.^{6, 12)}

Figures 2(a) and 2(b) show the isotropy in the magnetic susceptibility measured in a field of 1 T field and the isothermal magnetization at 2 K along crystallographic directions $\langle 100 \rangle$, $\langle 110 \rangle$, and $\langle 111 \rangle$, respectively. This is not unexpected considering the isotropically dense unit cell. The magnetization appears to be linear and attains a value of only

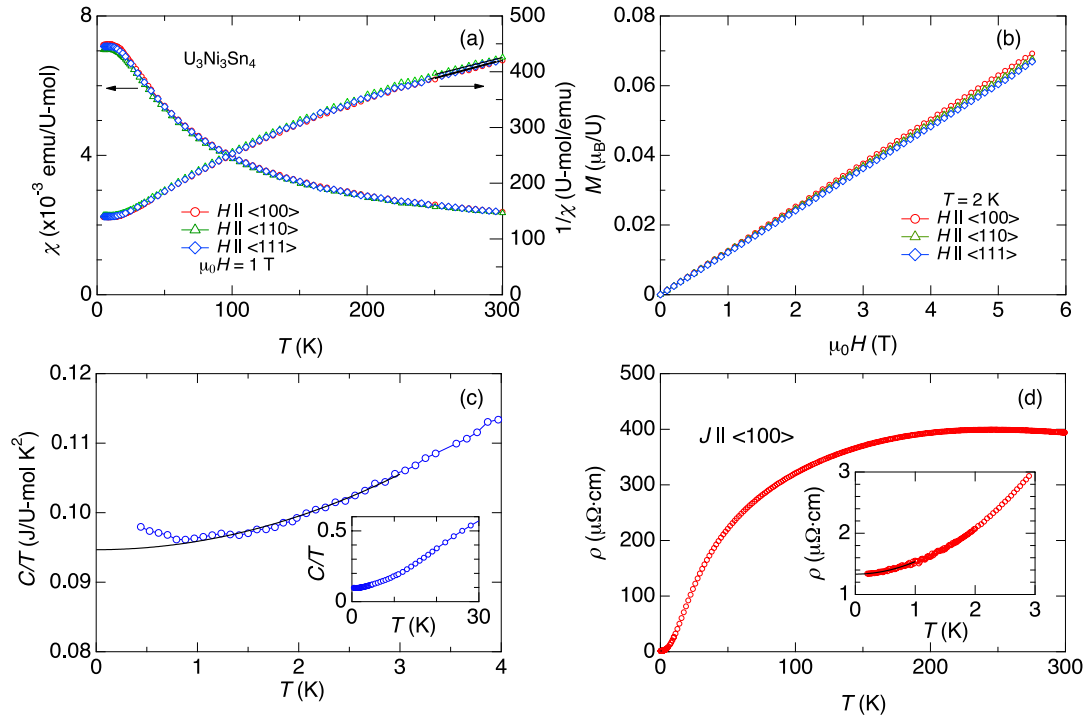


Fig. 2. (Color online) Physical properties as a function of temperature of single-crystal $\text{U}_3\text{Ni}_3\text{Sn}_4$: (a) magnetic susceptibility (left axis) and inverse susceptibility (right axis), (b) isothermal magnetization at 2 K, (c) specific heat, and (d) electrical resistivity. Solid black lines in panels (a), (c), (d) represent the fitted curves as discussed in the text.

Table I. Crystal data and structure refinement parameters of $\text{U}_3\text{Ni}_3\text{Sn}_4$ single crystal.

Parameter	Value
Structure prototype	$\text{Y}_3\text{Au}_3\text{Sb}_4$
Crystal system	cubic
Space group	$I\bar{4}3d$, #220, T_d^6
Z	4
Lattice parameter [Å]	$a = 9.3575(4)$
Radiation	MoK_α ($\lambda = 0.71073$ Å) (graphite monochromated)
Temperature [°C]	23.0
$\mu(\text{MoK}_\alpha)$ [mm^{-1}]	77.646
Calculated density [g cm^{-3}]	11.064
Scan mode	$\omega - 2\theta$
Measured reflections	1087
Independent reflections	253
Refinement	Full-matrix least-squares on F^2
$2\theta_{\text{max}}$	66.1°
Refined parameters	9
Extinction coefficient	0.0365
R1	0.027
wR2 (All reflections)	0.0903
Goodness-of-fit	1.074

Table II. Fractional atomic coordinates of $\text{U}_3\text{Ni}_3\text{Sn}_4$ as determined from single-crystal X-ray diffraction data.

Atoms	Wyckoff site	Site symmetry	x	y	z
U	12a	4	3/8	0	1/4
Ni	12b	4	7/8	0	1/4
Sn	16c	3	0.0820(2)	0.0820(2)	0.0820(2)

$\sim 0.07 \mu_B/\text{U}$ at 5.5 T. The susceptibility increases with decreasing temperature and saturates below 15 K to a value of

$\chi_0 \approx 7 \times 10^{-3} \text{ emu/U-mol}$. This behavior is reminiscent of the crossover from Curie to Pauli susceptibility below the Kondo temperature in Kondo lattice compounds. The inverse susceptibility (χ^{-1}) is a nonlinear function of temperature, although the Curie-Weiss law, $\chi^{-1} = (T - \theta_p)/C$ can be fitted in the temperature range 250–300 K, giving effective paramagnetic moment (μ_{eff}) values of 3.51, 3.63, and $3.50 \mu_B/\text{U}$ along the $\langle 100 \rangle$, $\langle 110 \rangle$, and $\langle 111 \rangle$ directions, respectively. The μ_{eff} values are comparable to those for the U^{3+} ($5f^3$) or U^{4+} ($5f^2$) configuration of the U ion.

Figure 2(c) shows the specific heat as a function of temperature $[C(T)]$ for $\text{U}_3\text{Ni}_3\text{Sn}_4$ at temperatures down to 0.4 K. Fitting the equation $C/T = \gamma + \beta T^2$ to the low-temperature data in the range 1 to 3 K gives the electronic specific heat coefficient (Sommerfeld coefficient) of $\gamma = 95 \text{ mJ/(U-mol K}^2\text{)}$, which is close to the values for a polycrystalline sample⁸⁾ and a single-crystal sample.¹³⁾ The small upturn below 1 K is also consistent with the previous results in a single crystal, although the C/T value here is slightly lower than the previous ones. This upturn is probably related to the crossover from the non-Fermi liquid to Fermi liquid regime around 0.4 K together with the nuclear contribution to the specific heat, as mentioned in Ref. 13.

Electrical resistivity as a function of the temperature, $\rho(T)$, of $\text{U}_3\text{Ni}_3\text{Sn}_4$ for $J \parallel \langle 100 \rangle$ is shown in Fig. 2(d). The resistivity follows the T^2 dependence below 1 K, and a least-squares fitting of the expression $\rho(T) = \rho_0 + AT^2$ gives residual resistivity $\rho_0 = 1.3 \mu\Omega \cdot \text{cm}$ and $A = 0.20 \mu\Omega \cdot \text{cm K}^{-2}$. The large value of coefficient A results a Kadowaki-Woods ratio (A/γ^2) of $2 \times 10^{-5} \mu\Omega \cdot \text{cm}(\text{mJ/K U-mol})^2$, which is slightly higher but not very far from the universal value [$1 \times 10^{-5} \mu\Omega \cdot \text{cm}(\text{mJ/K mol})^2$]. Also the Wilson ratio R_W , defined as $R_W = \pi^2 k_B^2 \chi_0 / (\gamma \mu_{\text{eff}}^2)$, for $\text{U}_3\text{Ni}_3\text{Sn}_4$ is 1.3, close to

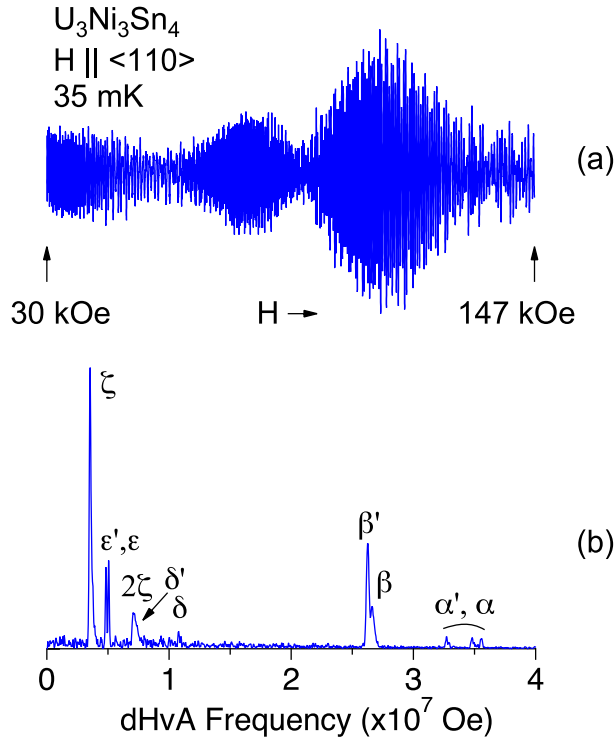


Fig. 3. (Color online) dHvA oscillations and corresponding FFT spectrum at 35 mK along $\langle 110 \rangle$ in $\text{U}_3\text{Ni}_3\text{Sn}_4$.

the free-electron value of unity. $\rho(T)$ at 300 K ($394 \mu\Omega \cdot \text{cm}$) in conjunction with the value of ρ_0 gives a residual resistivity ratio ($RRR = \rho_{RT}/\rho_0$) of 296, indicating the high quality of the grown $\text{U}_3\text{Ni}_3\text{Sn}_4$ crystal. The broad hump in $\rho(T)$ around 250 K may be attributed to the hybridization of U $5f$ electrons with the conduction electrons.

The angular dependence of dHvA oscillations was measured from $\langle 110 \rangle$ to $\langle 100 \rangle$ and from $\langle 100 \rangle$ to $\langle 111 \rangle$ then $\langle 110 \rangle$ by rotating the crystal in the $\{001\}$ and $\{110\}$ planes, respectively. The dHvA signal starts to appear from a small field of ~ 1.5 T, indicating the high quality of the present sample. Figure 3 shows the typical dHvA oscillations in the field range 3–14.7 T and the corresponding FFT spectra for the magnetic field parallel to the $\langle 110 \rangle$ crystallographic directions at 35 mK. dHvA oscillations of frequency components of up to $\sim 4 \times 10^7$ Oe were observed, which can be categorized into branches α , α' , β , β' , δ , δ' , ϵ , ϵ' , and ζ as fundamental dHvA branches.

The splitting of dHvA branches except for branch ζ is observed in Fig. 3. In general, the splitting of the dHvA frequency is often accounted for (a) similar extremal orbits of the same (often corrugated) Fermi surfaces, (b) spin-split Fermi surfaces with a small energy difference, (c) magnetic breakdown between two Fermi surfaces closely separated in energy, or (d) bicrystals with slightly misaligned grains. However, we observed a similar spectrum for a single-crystal obtained from a different batch. This leads us to conclude that the splitting in this case is primarily due to antisymmetric-SOC-induced lifting of the twofold spin degeneracy and the magnetic breakdown effect. The phenomena of magnetic breakdown occur when the energy gap between Fermi surfaces is small and electrons in the cyclotron orbits possess enough energy to tunnel or “break through” the gap at high magnetic fields. This

may modify the spectra of dHvA frequencies, which sometimes show forbidden orbits with extremal area larger than the Brillouin zone.²³⁾ Blount derived the criterion for magnetic breakdown as $\hbar\omega_C \gtrsim \epsilon_g^2/\epsilon_F$, where ω_C is the cyclotron frequency, ϵ_g is the energy gap, and ϵ_F is the Fermi energy.²⁴⁾ This condition can be easily realized for spin-split Fermi surfaces, particularly in high-symmetry cases. One recent example is TaSi_2 , in which two additional cyclotron orbits were detected by the magnetic breakdown originating from lack of an inversion center in its crystal structure.²⁵⁾

Figure 4(a) shows the dHvA frequencies as a function of sample orientation with respect to the magnetic field. Ten different dHvA branches, namely α , α' , β , β' , γ , δ , δ' , ϵ , ζ , and η , were detected. Most of the frequencies are nearly constant over a wide range of angles, which is expected for spherical Fermi surfaces. Under this scenario, branches α , α' , β , β' , γ , δ , δ' , ϵ , ζ , and η occupy 25%, 22%, 16%, 16%, 4.2%, 3.6%, 2.3%, 1.4%, 0.77%, and 0.17% of volume of the Brillouin zone, respectively.

In order to clarify the Fermi surfaces in $\text{U}_3\text{Ni}_3\text{Sn}_4$, we performed energy band structure calculations using the KANSAI code based on an FLAPW (full potential linear augmented plane wave) method with an LDA for the $5f$ -itinerant model. In the band calculations, the scalar relativistic effect was taken into account for all the electrons. The SOC was included as the second variational procedure for valence electrons. In the calculations, we used the structural parameters listed in Tables I and II. Core electrons (Rn-core minus $6s^26p^6$ electrons for U, Ar-core for Ni, Kr-core for Sn) were calculated inside muffin-tin spheres in each self-consistent step. $6s^26p^6$ electrons on U and $4d^{10}$ electrons on Sn were calculated as valence electrons by using a second energy window. The LAPW basis functions were truncated at $|k + G_i| \leq 9.20 \times 2\pi/a$, corresponding to 1601 LAPW functions. The sampling points were uniformly distributed to 506 k-points in the irreducible $1/24\text{th}$ of the Brillouin zone, which were divided by (20, 20, 20).

Figure 5 shows the calculated density of states (DOS) in $\text{U}_3\text{Ni}_3\text{Sn}_4$. The large DOS at the Fermi level is mainly due to the $5f$ electrons of U.

Figure 6 shows the band structure in $\text{U}_3\text{Ni}_3\text{Sn}_4$. It was found that many bands in the $J = 5/2$ manifold cross the Fermi level. Note that the bands near the Fermi level are eight-fold degenerated at the H point. In general, fourfold degeneracy can be found in high-symmetry points in the symmorphic space group of cubic systems. However, $\text{U}_3\text{Ni}_3\text{Sn}_4$ belongs to the non-symmorphic space group, therefore the degeneracy of many of its electronic states is doubled at the Brillouin zone boundary. Such high degeneracy might be the reason why many Fermi surfaces appear in $\text{U}_3\text{Ni}_3\text{Sn}_4$.

The calculated angular dependences of $\text{U}_3\text{Ni}_3\text{Sn}_4$ based on the LDA method are compared with the fundamental frequencies observed experimentally in Fig. 4(b). The theoretical angular dependences of dHvA frequencies are in reasonably good agreement with those obtained by experiments. Figure 7 shows the calculated Fermi surfaces in $\text{U}_3\text{Ni}_3\text{Sn}_4$. Twelve bands cross the Fermi energy and form the Fermi surfaces. All of them are closed Fermi surfaces with a nearly spherical shape.

One can recognize that the Fermi surfaces are paired. For instance, the band 253rd hole Fermi surface is paired with

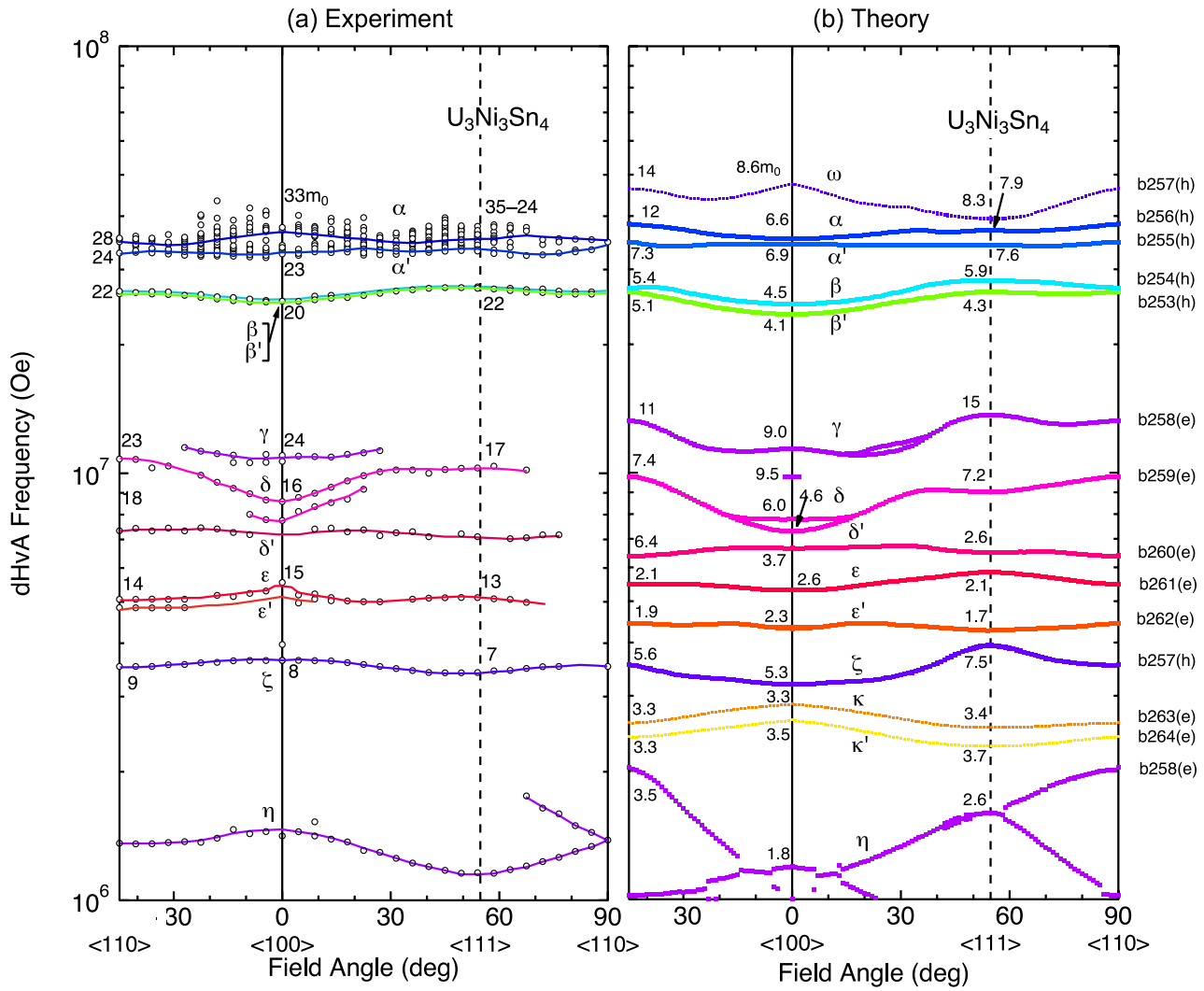


Fig. 4. (Color online) Angular dependence of the dHvA frequencies in $\text{U}_3\text{Ni}_3\text{Sn}_4$ obtained by (a) experiment and (b) theory based on the LDA band calculations. Cyclotron effective masses (a) and band masses (b) are also shown as numbers for $H \parallel \langle 100 \rangle$, $\langle 110 \rangle$, and $\langle 111 \rangle$. The thick solid lines in panel (b) correspond to the experimentally detected dHvA branches. The annotations at the right side in panel (b) indicate the band number and the hole/electron Fermi surface. For instance, “b256(h)” corresponding to branch α indicates the band 256th hole Fermi surface.

the band 254th hole Fermi surface, meaning that the original band with spin degeneracy splits into two bands due to the antisymmetric spin-orbit interaction in the non-centrosymmetric crystal structure.

The comparison between experiments and theory is summarized as follows.

- (1) Branches α and α' correspond to the band 256th and 255th hole Fermi surfaces centered at the H point, respectively. Many dHvA frequencies were detected near branches α and α' in Fig. 4(a). This is most likely due to the magnetic breakdown between α and α' .
- (2) Branches β and β' correspond to the band 254th and 253rd hole Fermi surfaces centered at the H point, respectively.
- (3) Branch γ originates from the band 258th electron Fermi surface centered at the Γ point. The dHvA frequency was detected only for the field close to the $\langle 100 \rangle$ direction, probably due to the curvature factor.
- (4) Branches δ and δ' are due to the band 259th and 260th electron Fermi surfaces centered at the Γ point. Since the Fermi surface of the band 259th is slightly corrugated compared with the spherical shape, the dHvA frequency splits near $H \parallel \langle 100 \rangle$.
- (5) Branches ϵ and ϵ' are ascribed to the band 261st and 262nd electron Fermi surfaces centered at the Γ point, respectively.
- (6) Branch ζ is due to the band 257th hole Fermi surface centered at the P point.
- (7) Branch η originates from the small pocket Fermi surface centered at the N point in the 258th band.
- (8) Branch ω originates from the largest hole Fermi surface centered at the H point in the 257th band. This Fermi surface was not detected experimentally, probably due to the large cyclotron effective mass.
- (9) Branches κ and κ' originates from the band 263rd and 264th electron Fermi surfaces centered at the Γ point, respectively. These Fermi surfaces were not experimentally detected.

Note that in Fig. 6, the splitting bands and their pairs are not very clear, and they are rather complicated, crossing each

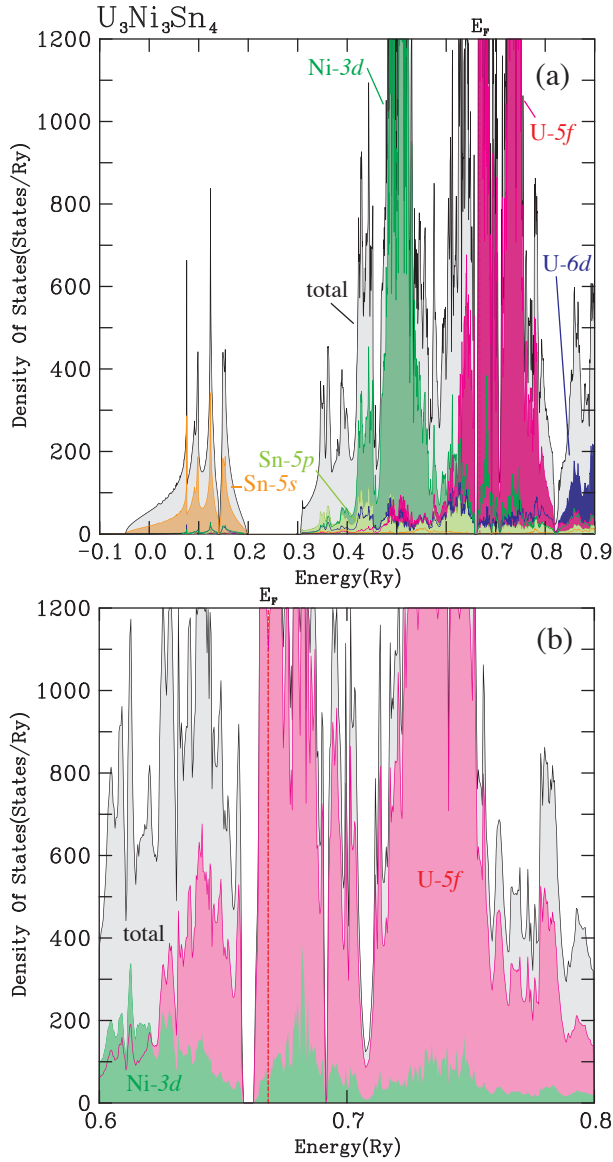


Fig. 5. (Color online) Calculated density of states for $\text{U}_3\text{Ni}_3\text{Sn}_4$ (a) in whole energy region and (b) near the Fermi level. The partial components inside the muffin-tin spheres are also shown.

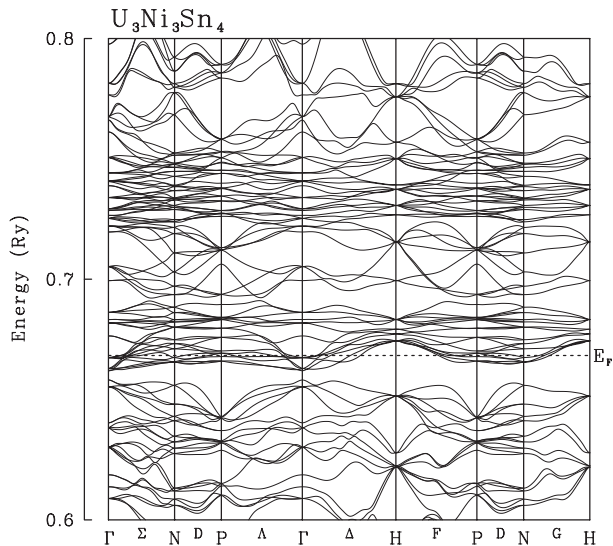


Fig. 6. Calculated band structure near the Fermi level. The $J = 5/2$ bands of $5f$ electrons in U are located in the vicinity of the Fermi level. The $J = 7/2$ bands are around 0.74 Ry. See also Fig. 5(b).

Table III. Experimental dHvA frequency F , cyclotron effective mass m_c^* , calculated dHvA frequency F_b and band mass m_b in $\text{U}_3\text{Ni}_3\text{Sn}_4$.

Branch	Experiment		Theory	
	F ($\times 10^6$ Oe)	m_c^* (m_0)	F_b ($\times 10^6$ Oe)	m_b (m_0)
$H \parallel \langle 100 \rangle$				
ω			47.5	8.6
α	37.6	33	35.4	6.6
α'	32.6	23	34.4	6.9
β	25.3	20	24.8	4.5
β'			23.5	4.1
γ	11.0	24	11.4	9.0
			9.78	9.5
δ	8.58	16	7.78	6.0
			7.29	4.6
δ'			6.65	3.7
ϵ	5.55	15	5.32	2.6
ϵ'			4.34	2.3
ζ	3.65	8	3.20	5.3
κ			2.87	3.3
κ'			2.63	3.5
η	1.41		1.19	1.8
$H \parallel \langle 110 \rangle$				
ω			46.4	14
α	34.8	28	38.3	12
α'	32.8	24	34.7	7.3
β	26.7	22	27.1	5.4
β'	26.3		26.6	5.1
γ			13.2	11
δ	10.8	23	9.79	7.4
δ'	7.33	18	6.39	6.4
ϵ	5.07	14	5.48	2.1
ϵ'	4.84		4.41	1.9
ζ	3.53	9	3.55	5.6
κ			2.59	3.3
κ'			2.40	3.3
η	1.36		2.04	3.5
$H \parallel \langle 111 \rangle$				
ω			39.6	8.3
α	38.3–33.7	35–24	37.0	7.9
α'			34.1	7.6
β	27.3	22	28.2	5.9
β'	27.1		26.5	4.3
γ			13.7	15.1
δ	10.3	17	9.01	7.2
δ'	7.10		6.51	2.6
ϵ	5.11	13	5.85	2.1
ϵ'			4.27	1.7
ζ	3.41	7	3.94	7.5
κ			2.53	3.4
κ'			2.29	3.7
η	1.16		1.59	2.6

other. In reality, the manifold of $5f$ bands in U splits and forms 12 bands crossing the Fermi level because of the antisymmetric SOC in the non-centrosymmetric structure.

In order to determine the cyclotron effective mass, we measured the temperature dependence of the dHvA amplitude in the range 35–200 mK along $\langle 100 \rangle$, $\langle 110 \rangle$, and $\langle 111 \rangle$. Rapid suppression of the dHvA amplitude revealed the enhanced effective mass m_c^* . We deduced values of m_c^* ranging from 7 to 35 m_0 in $\text{U}_3\text{Ni}_3\text{Sn}_4$, where m_0 is the rest mass of an electron. The large cyclotron effective mass indicates that $\text{U}_3\text{Ni}_3\text{Sn}_4$ is a heavy-fermion compound. These values are compared with the band mass in Table III. The cyclotron effective masses are larger than the corresponding band masses with the ratio $m_c^*/m_b \sim 1$ –6. For example, the cyclotron ef-

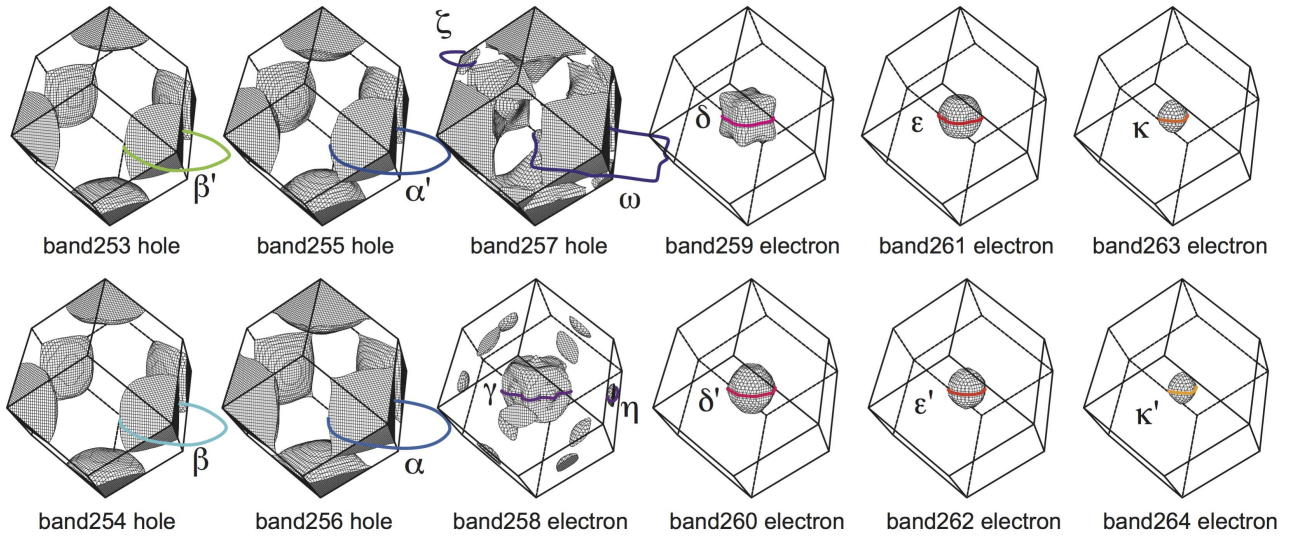


Fig. 7. (Color online) Calculated Fermi surfaces in the bcc Brillouin zone of $\text{U}_3\text{Ni}_3\text{Sn}_4$.

fective mass of branch α , which has the largest Fermi surface detected experimentally, is five times larger than the band mass for $H \parallel \langle 100 \rangle$. The electronic specific heat coefficient [$\gamma \sim 95 \text{ mJ}/(\text{K}^2\text{U-mol})$] is five times larger than that obtained from the band calculation [$\gamma_b \sim 19.6 \text{ mJ}/(\text{K}^2\text{U-mol})$]; thus, the mass enhancement for the dHvA branch is roughly consistent with the enhancement of the γ -value.

For a spherical Fermi surface, the electronic specific heat coefficient (γ -value) is described as $\gamma = \frac{\pi^2}{3} k_B^2 D(\epsilon_F) = (k_B^2 V / 6\hbar^2) m_c^* k_F$, where $D(\epsilon_F)$ is the DOS at the Fermi level, k_F is half of the caliper dimension of the Fermi surface, and V is the molar volume of $\text{U}_3\text{Ni}_3\text{Sn}_4$. Note that the spin degeneracy is not taken into account here because of the lack of inversion symmetry in the crystal structure.

Assuming spherical Fermi surfaces, the values of γ derived for various dHvA frequencies vary between 1 and 13 $\text{mJ}/(\text{U-mol K}^2)$. The sums of the values of γ in $\langle 100 \rangle$, $\langle 110 \rangle$, and $\langle 111 \rangle$ amount to 36, 35, and 33 $\text{mJ}/(\text{U-mol K}^2)$, respectively, which are smaller than the experimentally determined value of 95 $\text{mJ}/(\text{U-mol K}^2)$. For $H \parallel \langle 100 \rangle$, the missing Fermi surface ω will give 17 $\text{mJ}/\text{K}^2\text{U-mol}$, assuming the same mass enhancement of branch α , that is, $m_c^*/m_b \sim 5$. The other undetected Fermi surfaces, namely β' , δ' , ϵ' , κ , κ' , and η , will give approximately 15 $\text{mJ}/\text{K}^2\text{U-mol}$. Therefore the γ -value amounts to $\sim 70 \text{ mJ}/\text{K}^2\text{U-mol}$ in total, which is roughly consistent with the γ -value obtained by specific heat measurements.

According to the Lifshitz-Kosevich formula, the field dependence of the amplitude of dHvA oscillations at a constant temperature T is given by

$$\ln \left[A H^{1/2} \sinh(\lambda m_c^* T / H) / J_2(x) \right] = -\lambda m_c^* T_D \cdot \frac{1}{H} + \text{const.},$$

where A is the dHvA amplitude, T_D is the Dingle temperature, λ is defined as $\lambda = 2\pi^2 c k_B / e\hbar$, and $J_2(x)$ is the Bessel function due to the field modulation technique with $x = 2\pi F h / H^2$. In Fig. 8 we have constructed a Dingle plot by displaying $1/H$ vs $\ln \left[A H^{1/2} \sinh(\lambda m_c^* T / H) / J_2(x) \right]$ for the main dHvA branches α , α' , and β at 35 mK for $H \parallel \langle 100 \rangle$ data. From the slope of the Dingle plot, we derived T_D , which gives an average scat-

tering lifetime $\tau = \hbar / (2\pi k_B T_D)$. Knowing τ and k_F , the mean free path of electrons can be estimated by $l = \hbar k_F \tau / m_c^*$. We deduce Dingle temperatures of 103, 101, and 102 mK corresponding to mean free paths of 1903, 1904, and 1950 Å for the α , α' , and β branches, respectively. The low Dingle temperature and large mean free path indicate that $\text{U}_3\text{Ni}_3\text{Sn}_4$ is a clean system with minimal atomic disorder, impurity concentration, or crystal defects.

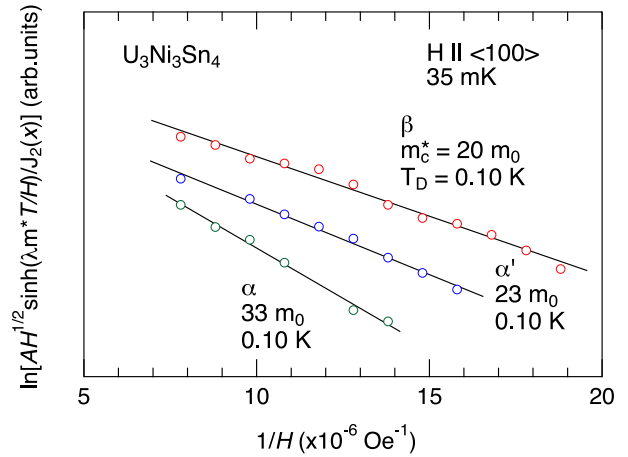


Fig. 8. (Color online) Dingle plot of $\text{U}_3\text{Ni}_3\text{Sn}_4$ for $H \parallel \langle 100 \rangle$ at 35 mK.

Now we evaluate the splitting energy, which corresponds to the magnitude of the antisymmetric spin-orbit interaction, from the simple relation^{26–28)}

$$\Delta\epsilon = \frac{\hbar e}{m_c^* c} \Delta F, \quad (1)$$

where ΔF is the frequency difference between two splitting branches. We obtain $\Delta\epsilon = 24 \text{ K}$ for branches α , α' for $H \parallel \langle 100 \rangle$ and $\Delta\epsilon = 23 \text{ K}$ for branches δ , δ' for $H \parallel \langle 110 \rangle$.

Here we used the cyclotron effective mass m_c^* to deduce the splitting energy. In the band structure calculations, the band mass is obtained from $m_b = \hbar^2 / 2\pi(\Delta S / \Delta\epsilon)$, where S is the

cross-sectional area of the Fermi surface. Thus, the splitting energy can be derived using the band mass instead of the cyclotron effective mass. In this case, we obtained $\Delta\varepsilon = 100$ and 68 K for branches α , α' ($H \parallel \langle 100 \rangle$) and branches δ , δ' ($H \parallel \langle 110 \rangle$), respectively.

These values are small compared with those for other materials without inversion symmetry. In VSi_2 , NbSi_2 and TaSi_2 which have a chiral structure, the splitting energy has been estimated to be 20–100, 200–300, and 500–600 K, respectively from experiments. The splitting energy is dependent on the d -electron, and the $5d$ -electrons in TaSi_2 produce the largest splitting energy. A similar trend also occurs in LaTGe_3 ($\text{T}=\text{Co, Rh, Ir}$). Naively thinking, it can be inferred that $\text{U}_3\text{Ni}_3\text{Sn}_4$ has a large splitting energy, because of the $5f$ and $6d$ -electrons in the U atom. However, the present results for $\text{U}_3\text{Ni}_3\text{Sn}_4$ imply that the splitting energy is strongly reduced by the large cyclotron mass or the band mass.

Note that we assumed the splitting bands are paired, such as α and α' , δ and δ' , for simplicity. However, the adjoining bands are not simply paired, as shown in Fig. 6, because the interband distances are not sufficiently larger than the spin-splitting. Thus, it is not simple to derive the splitting energy from the experiment.

4. Summary

We succeeded in growing high quality single crystals of $\text{U}_3\text{Ni}_3\text{Sn}_4$ without inversion symmetry in the crystal structure. The resistivity, specific heat, and magnetic susceptibility revealed that $\text{U}_3\text{Ni}_3\text{Sn}_4$ is a paramagnetic heavy-fermion compound in the proximity of the quantum critical point. The dHvA experiments showed that the Fermi surfaces consist of closed ones, and the angular dependence of the dHvA frequency is in reasonably good agreement with the LDA band calculations based on the $5f$ -itinerant model. To our knowledge, this is the first time that the splitting of Fermi surfaces due to the lack of inversion symmetry has been clearly detected in $5f$ electron systems. The large cyclotron effective mass of up to $35 m_0$ indicates the heavy electronic state in $\text{U}_3\text{Ni}_3\text{Sn}_4$. The small splitting energy is probably related to the heavy quasi-particles in $\text{U}_3\text{Ni}_3\text{Sn}_4$.

Acknowledgements

We thank Y. Ōnuki, A. de Visser, N. Kimura, and V. P. Mineev for fruitful discussions. This work was supported by KAKENHI (JP15H05882, JP15H05884, JP15K21732, JP15H05745, JP16H04006, JP15K05156, JP16K17733, JP17K14328).

- 1) V. Sechovsky and L. Havela, in *Handbook of Magnetic Materials*, eds. K. H. J. Buschow, (Elsevier Science Publishers, 1998) Vol.11, Chapter 1.
- 2) D. Aoki and J. Flouquet, J. Phys. Soc. Jpn. **81** 011003 (2012).
- 3) J.M. Fournier and E. Gratz, in *Handbook on the Physics and Chemistry of rare earths*, eds. K.A. Gschneidner, Jr. L. Eyring, G.H. Lander and G.R. Choppin (Elsevier Science Publishers, 1993) Vol.17.
- 4) K. T. Moore, and G. van der Laan, Rev. Mod. Phys. **81**, 235 (2009).
- 5) P. Santini, S. Carretta, G. Amoretti, R. Caciuffo, N. Magnani, and G. H. Lander, Rev. Mod. Phys. **81**, 807 (2009).
- 6) A. E. Dwight, J. Nucl. Mater. **79**, 417 (1979).
- 7) T. Endstra, G. J. Nieuwenhuys, J. A. Mydosh, and K. H. J. Buschow, J. Magn. Magn. Mater. **89**, L273 (1990).
- 8) T. Takabatake, S. Miyata, H. Fujii, Y. Aoki, T. Suzuki, T. Fujita, J. Sakurai, and T. Hiraoka, J. Phys. Soc. Jpn. **59**, 4412 (1990).
- 9) T. Takabatake, S. Miyata, H. Fujii, Y. Aoki, T. Suzuki, and T. Fujita, Physica B **165&166**, 437 (1990).
- 10) P. C. Canfield, A. Lacerda, J. D. Thompson, G. Sparn, W. P. Beyermann, M. F. Hundley, and Z. Fisk, J. Alloys Compd. **181**, 77 (1992).
- 11) T. Klimczuk, Han-oh Lee, F. Ronning, T. Durakiewicz, N. Kurita, H. Volz, E. D. Bauer, T. McQueen, R. Movshovich, R. J. Cava, and J. D. Thompson, Phys. Rev. B **77**, 245111 (2008).
- 12) L. Shlyk, J. C. Waerenborgh, P. Estrela, L. E. De Long, A. de Visser, and M. Almeida, J. Phys.: Condens. Matter **11**, 3525 (1999).
- 13) L. Shlyk, J.C. Waerenborgh, L.E. De Long, A. de Visser, D.P. Rojas, F. Gandra, and M. Almeida, Physica B **292**, 89 (2000).
- 14) S.-H. Baek, N. J. Curro, T. Klimczuk, H. Sakai, E. D. Bauer, F. Ronning, and J. D. Thompson, Phys. Rev. B **79**, 195120 (2009).
- 15) Y. Inada, P. Wiśniewski, M. Murakawa, D. Aoki, K. Miyake, N. Watanabe, Y. Haga, E. Yamamoto, and Y. Ōnuki, J. Phys. Soc. Jpn. **70**, 558 (2001).
- 16) P. Estrela, A. de Visser, F. R. de Boer, T. Naka, and L. Shlyk, Phys. Rev. B **63**, 212409 (2001).
- 17) A. de Visser, P. Estrela, and T. Naka, Int. J. Mod Phys B **16**, 2998 (2002).
- 18) C. H. Booth, L. Shlyk, K. Nenkov, J. G. Huber, and L. E. De Long, Phys. Rev. B **69**, 104430 (2004).
- 19) T. Takabatake, S. Miyata, H. Fujii, K. Yokoyama, and M. Taniguchi, Solid State Commun. **81**, 433 (1992).
- 20) T. Endstra, G. J. Nieuwenhuys, K. H. J. Buschow, and J. A. Mydosh, J. Magn. Magn. Mater. **108**, 69 (1992).
- 21) K. Kojima, Y. Hukuda, S. Miyata, T. Takabatake, H. Fujii, and T. Hihara, J. Phys. Soc. Jpn. **60**, 2546 (1991).
- 22) T. Ejima, Y. Kudo, S. Suzuki, T. Takahashi, S. Sato, T. Kasuya, T. Takabatake, and T. Ishii, Physica B **186-188**, 86 (1993).
- 23) D. Shoenberg, in *Magnetic Oscillations in Metals*, (Cambridge University Press, 1984).
- 24) E. I. Blount, Phys. Rev. **126**, 1636 (1962).
- 25) A. Nakamura, H. Harima, M. Hedo, T. Nakama, and Y. Ōnuki, J. Phys. Soc. Jpn. **82**, 113705 (2013).
- 26) Y. Ōnuki, A. Nakamura, T. Uejo, A. Teruya, M. Hedo, T. Nakama, F. Honda, and H. Harima, J. Phys. Soc. Jpn. **83**, 061018 (2014).
- 27) V. P. Mineev and K. V. Samokhin, Phys. Rev. B **72**, 212504 (2005).
- 28) T. Terashima, M. Kimata, S. Uji, T. Sugawara, N. Kimura, H. Aoki, and H. Harima, Phys. Rev. B **78**, 205107 (2008).